Research paper

Achromatic Talbot lithography with nano-ring masks for high-throughput periodic patterning

Dimitrios Kazazis*, Li-Ting Tseng, Yasin Ekinci

Paul Scherrer Institute, 5232, Villigen-PSI, Switzerland

ABSTRACT

Periodic patterning is important for various scientific and technological applications, especially in the nanoscale. Achromatic Talbot lithography (ATL) utilizing extreme ultraviolet (EUV) wavelengths, notably 13.5 nm, is a powerful lithographic technique enabling high-resolution and high-throughput nanopatterning over large areas. Improving the resolution and the throughput of the technique requires elaborate designs based on simulations and nanofabrication of transmission diffraction gratings on thin silicon nitride membranes. Our simulations point to the fact that compared to conventional ATL masks with hole arrays, masks consisting of annular rings and intersecting annular rings show increased performance in terms of throughput. A set of masks with uncrossed and crossed annular rings have been nanofabricated and exposed with spatially coherent synchrotron EUV light and the experimental results confirm our theoretical predictions that masks with annular rings and crossed rings yield dot arrays with improved throughput. The presented technique may enable applications in science and technology where large-area and periodic nanopatterning is needed.

1. Introduction

Pushing the limits of lithographic patterning further into the nanoscale and towards single-digit nanometer resolution has been a central research topic mainly driven by the microelectronic industry for the high-volume manufacturing of microchips. This capability to pattern at the nanoscale has, in turn, enabled research in numerous other fields of science and technology. In many of these cases the patterns need to be periodically repeated as, for example, in plasmonic [1] and photonic [2] devices, magnetic media [3], solar cells [4], directed self-assembly [5], antibacterial surfaces [6], and photoresist testing [7]. Achromatic Talbot lithography (ATL) or achromatic spatial frequency multiplication (ASFM) is a nanopatterning technique with inherent periodicity and when it is combined with extreme ultraviolet (EUV) wavelengths, it can produce periodic patterns at the nanoscale [8].

The EUV ATL method has several advantages compared to other lithographic techniques. First, as a photolithography technique, it is parallel and therefore more efficient than any other high-resolution, direct-write technique [9]. At the same time, it is characterized by frequency multiplication (which explains the ASFM name): The patterns recorded on the photoresist have a smaller pitch than the patterns on the mask, for example by a factor of 2 for line/space patterns and a factor of $\sqrt{2}$ for pillars or contact-hole arrays [10]. In addition, the use of EUV light enables patterning at the nanoscale due to the short

wavelength of 13.5 nm. Another advantage of employing EUV light is the several related technologies that have been developed for high-volume manufacturing with EUV lithography, such as light sources and photoresists. For example, EUV ATL using a broadband plasma source has been successfully demonstrated, taking also advantage of the achromatic nature of the ATL method [11,12]. Moreover, due to the nature of the aerial image generated by ATL, it has a very large depth-of-focus, enabling for example patterning on surfaces with curvature or three-dimensional topographical features. Furthermore, compared to other interference lithography techniques, in ATL only one grating is used on the mask. This has a twofold benefit. First, all the diffracted light contributes to the aerial image and therefore the exposures are highly efficient. Second, there are no undesirable diffraction orders transmitted and recorded on the photoresist. This enables large area patterning by step-and-repeat. Nevertheless, we note that there are significant stitching errors in the step-and-repeat approach and therefore large-area applications are limited to those that are insensitive to stitching errors. Another advantage is that ATL is forgiving to local defects on the transmission masks, which is known as the self-healing property of ATL [10,13]. Last, the duty cycle of the printed periodic patterns can be modified by adjusting the exposure dose due to the triangular intensity profiles that lead to a constant aerial image contrast. All these advantages make ATL a powerful method for fabrication

---

* Corresponding author.
  E-mail address: dimitrios.kazazis@psi.ch (D. Kazazis).

of high-resolution periodic nanostructures with high throughput over large areas for a plethora of applications.

In our previous work [10] we investigated ways of improving the resolution and throughput of ATL by extensive simulations of different mask patterns. We found that by using annular rings instead of circular holes on the masks we still obtain arrays of dots in our aerial image with equally narrow intensity peaks, but with much larger absolute intensities. The intensity peak width was found to depend on the width of the annular ring, while the peak intensity increased with increasing ring diameter. Last, the pitch of the obtained dots in the aerial image depended on the pitch of the annular rings (divided by $\sqrt{2}$) exactly like in the case of a mask with holes.

In this paper, we investigate a way to improve the throughput as well as the resolution and density (pitch) of the ATL technique. We further simulate masks with rings and also rings that are crossing (pitch ≤ diameter) and investigate the performance and limitations of such masks. Moreover, we demonstrate the successful fabrication of masks with crossed and uncrossed rings of several sizes and pitches and we present experimental results from EUV exposures. We start in section 2 by briefly presenting the theory of ATL along with simulations of several different mask designs. In section 3 we present the experimental methods and materials used for the nanofabrication of the transmission masks and in section 4 the experimental results obtained at EUV exposures at the Swiss light source (SLS). Finally, we present our main conclusions and discuss the outlook of our research on improved resolution and throughput.

2. Theory and simulations

When a diffraction grating is illuminated by coherent monochromatic light, self-images of the grating appear at well-defined distances from the grating [14,15]:

$$Z_{T,n} = \frac{2p^2}{\lambda}n, \tag{1}$$

where $Z_{T,n}$ are the Talbot distances, p is the grating period, λ is the wavelength, and n is an integer number. At rational multiples of Z_T, phase-shifted images or images with smaller period are also obtained, resulting in a fractal pattern known as the Talbot carpet. As the Talbot distances are generally small and the self-images have very limited depth-of-focus, it is impractical to use the Talbot effect for lithography.

However, in the quasimonochromatic case, where the grating is illuminated with light at $\lambda \pm \Delta\lambda$ wavelengths, a stationary intensity pattern is obtained [10] at distances beyond the so-called achromatic Talbot distance:

$$Z_A = \frac{2p^2}{\Delta\lambda} \tag{2}$$

As $Z_A \gg Z_T$ and as the stationary image has a large depth-of-focus, the ATL technique is practical for lithography, especially in the case of synchrotron illumination, where the large spatial coherence of the light (several millimeters) does not limit the extent of the stationary image, as explained in Ref. [8].

In our previous work, we have described how the aerial images of ATL can be simulated in a relatively simple manner by assuming plane wave illumination and calculating the propagation of the light diffracted by the transmission mask gratings. The simulations presented in this paper have been performed in the MATLAB numerical computing environment (MathWorks, Inc.) as described in our previous work [10].

In the following, we concentrate on simulating aerial images obtained by masks with annular ring gratings. In all the simulations to follow, the aerial images were calculated at a distance $z = 2Z_A$ from the mask to ensure that the distance is within the achromatic Talbot (stationary intensity) regime. As already discussed in Section 1, denser structures (dot or hole arrays) can be obtained by reducing the pitch of the rings. Our simulations show that even in the case that the rings
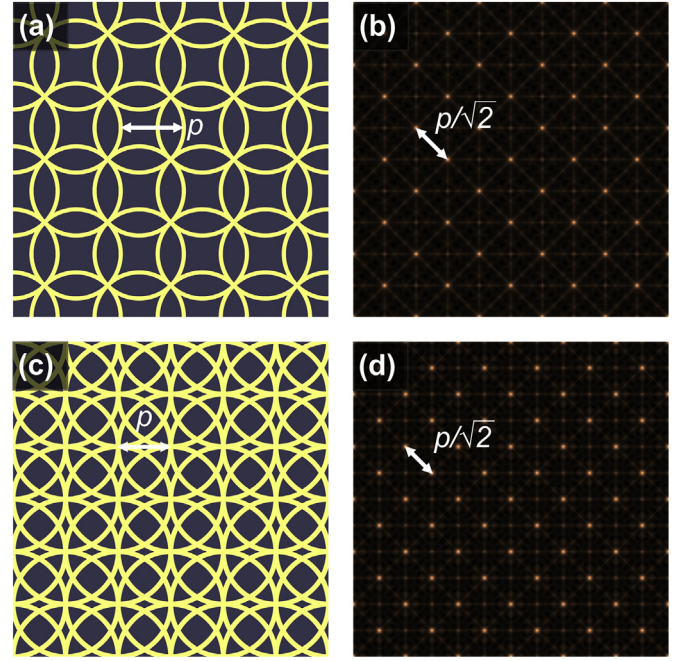
Fig. 1. Mask layouts (a) and (c) and simulated aerial images (b) and (d) of transmission gratings consisting of crossed annular rings with a pitch smaller than the rings' diameter. In both cases the aerial image is a square array of dots rotated by 45 ° and a pitch divided by $\sqrt{2}$. In (a) $p = d/\sqrt{2}$ and in (c) $p = d/2$ where d is the diameter of the ring.

touch or even cross, an aerial image of dots is obtained rotated by 45° and with a pitch divided by $\sqrt{2}$. This is shown in the simulations of Fig. 1, where two different masks with crossed rings (pitch < ring diameter) are simulated. The first mask shown in Fig. 1 (a) comprises rings with a pitch equal to the diameter of the ring divided by $\sqrt{2}$ and the second one shown in Fig. 1 (c) comprises denser rings with a pitch equal to the diameter of the ring divided by 2. As we see in the simulations shown in Figs. 1 (b) and (d) respectively, the aerial images consist of an array of sharp dots (intensity peaks) rotated by 45° and with a pitch equal to the ring pitch divided by $\sqrt{2}$. The mask of the densely-packed ring array can look very different than its aerial image of small sharp dots, which seems counterintuitive. This aerial image is, however, still very similar to that of a mask with hole arrays. Based on these simulations, we conclude that we can reduce the dot pitch in the aerial image simply by reducing the pitch of the crossed rings. As it will appear in the following, this is true to some extent, but there is a limit to how densely we can pack the annular rings on our masks. It is clear from Figs. 1 (a) and (b) that the denser we pack the rings, the more transparent (yellow area) the mask is. The extreme limit would be a fully transparent mask that should show no sharp intensity peaks arranged in a 45° rotated square array.

To verify this, we ran a series of simulations of masks with rings of a given diameter and width, but with varying pitch. The rings have an inner/outer diameter of 500/550 nm. This corresponds to a ring width of 25 nm. The simulated pitches of the rings were 525 nm (barely touching rings), 371 nm, 263 nm, 186 nm, 131 nm and 120 nm as in Figs. 2 (a) and (b). As we can see in the simulated aerial images shown in Fig. 2 (c), intensity peaks are observed in all the cases, in a 45° rotated square array arrangement, similar to Figs. 1 (b) and (d). These dots or intensity peaks are visible even for the pitch of 120 nm, where the mask is mostly transparent (yellow region). By applying a proper threshold to the intensities of these aerial images (after normalization), we can obtain the binary images of Fig. 2 (d). From an experimental point of view, applying a threshold is equivalent to adjusting the exposure dose. However, a deeper examination of the aerial image intensities reveals that the background intensity increases with
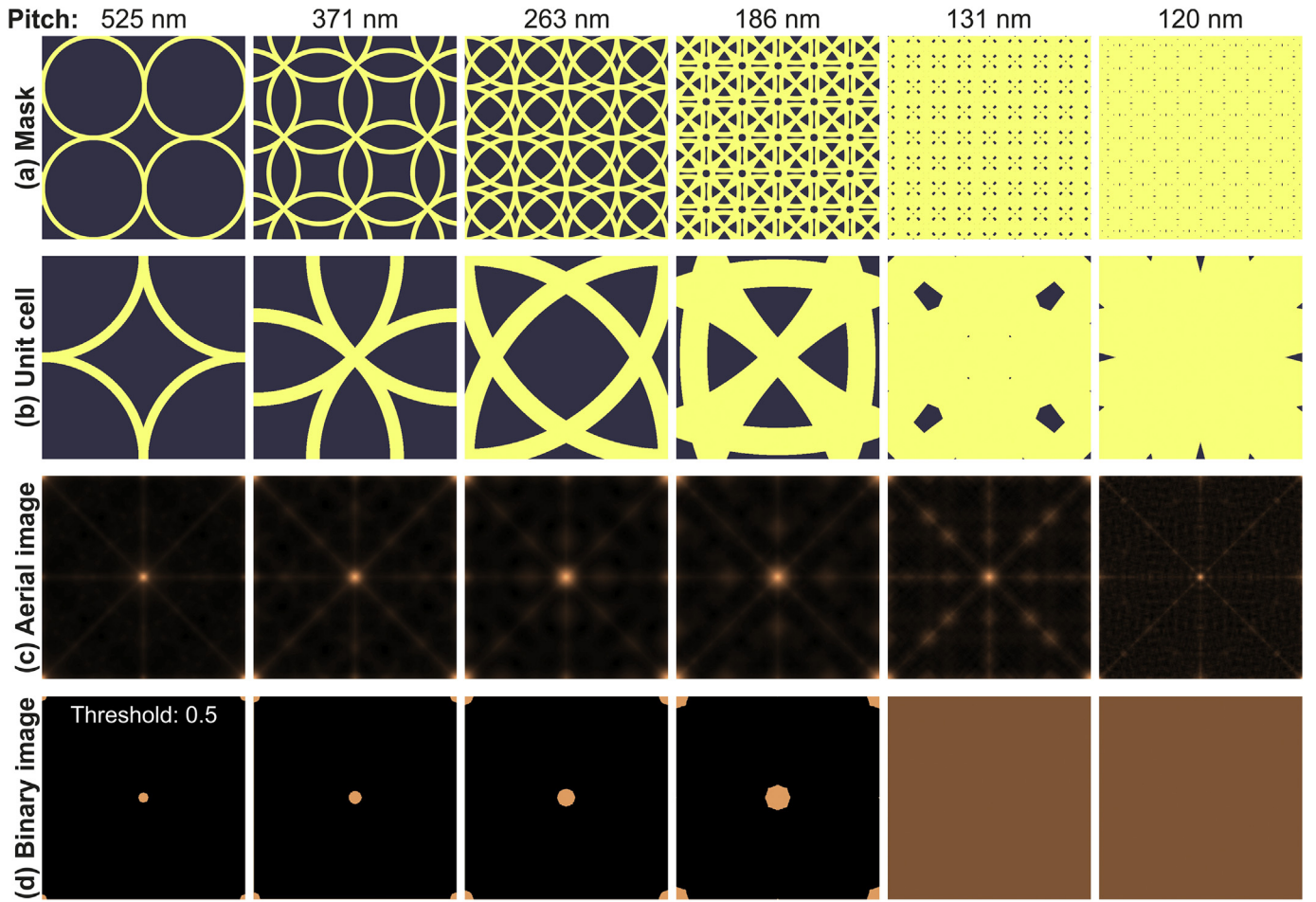
Fig. 2. Simulations of masks with rings of varying pitch. In all the masks the ring outer diameter is 550 nm and the inner one 500 nm. The ring width is always 25 nm. (a) Comparison of the mask layout using the same scale for all the pitches (square size 1050 nm). (b) The unit cells of the masks in (a) used in the simulations. (c) The simulated aerial images and for the masks in (b), obtained at a distance $z = 2z_A$ well within the achromatic regime. (d) Binary images obtained by applying a 50% threshold to the intensity of the aerial image. For 131 nm and 120 nm pitch the background intensity is already above the chosen threshold. The square size for (b), (c), and (d) is equal to the respective pitch.

decreasing pitch. This is immediately evident in the binary images where for the 131 and 120 nm pitches the background intensity is already above the threshold of 0.5 (no patterns on the resist).

Fig. 3 shows this effect clearly, where in Fig. 3 (a) the intensity of the central peak is plotted along the horizontal axis and in Fig. 3 (b) the image contrast as a function of the pitch is shown. The contrast in this context is defined as:

$$Contrast = \frac{I_{max} - I_{min}}{I_{max} + I_{min}} \qquad (3)$$

where I_{max} and I_{min} are the maximum and minimum intensities in the aerial image, respectively. We observe that the effect of decreasing the pitch is twofold. First, we observe an increase in the background with decreasing pitch, which is attributed to the larger transparent area on the mask for the denser ring arrays. Second, the maximum of the intensity originally increases for decreasing pitch and finally it decreases as well. This is understood as a weaker constructive interference of the diffracted orders, caused by the high density of the rings and the resulting disappearance of fine structures on the mask. The combined effect of the increased background and the decreased intensity maximum is better visualized in Fig. 3 (b), where the image contrast is shown. It is clear that the contrast decreases with decreasing pitch and as expected for mostly transparent masks, the contrast finally approaches 0. This is undesirable and impractical for lithography, where a sufficiently high contrast in the aerial image is essential for well-defined

and high-resolution patterns.

Qualitatively, this happens because with the decreasing pitch, by packing the rings denser together, some fine structures on the mask are lost with respect to ideal rings (of minimal width) and their position due to the overlapping areas. Therefore, one way to recover this information is by making the rings more "ideal" i.e. reducing their width. In Fig. 4 (a) the layouts of masks with crossed rings are shown. In all the layouts the rings have a mean diameter of 525 nm and a pitch of 131 nm which results in a pitch of 93 nm on the wafer, and the width of the rings is varying from 25 nm down to 5 nm. Already from the mask layouts, it is evident that as the ring width decreases, more detail is encoded into the mask layout. As it appears from the simulated intensity profiles of the dots, shown in Fig. 4 (b), the smaller ring widths result into higher and sharper intensities. This results, in turn, in increased contrast for the narrower rings as is shown in Fig. 4 (c) and at the same time in smaller obtained dots, if we compare the full width at half maximum (FWHM) of the normalized intensities. These FWHM values are also plotted in Fig. 4 (c) for the 3 smallest ring widths, 5, 10, and 15 nm. For larger ring widths the contrast is too low and it is not possible to define the FWHM values.

To summarize the advantages of masks with rings instead of holes, it is clear that large rings need lower exposure doses and thus show higher throughput. As discussed in this section, the pitch of the ring determines the pitch of the printed dots and denser arrays of dots can be achieved by crossing the rings on the mask. Furthermore, the width of
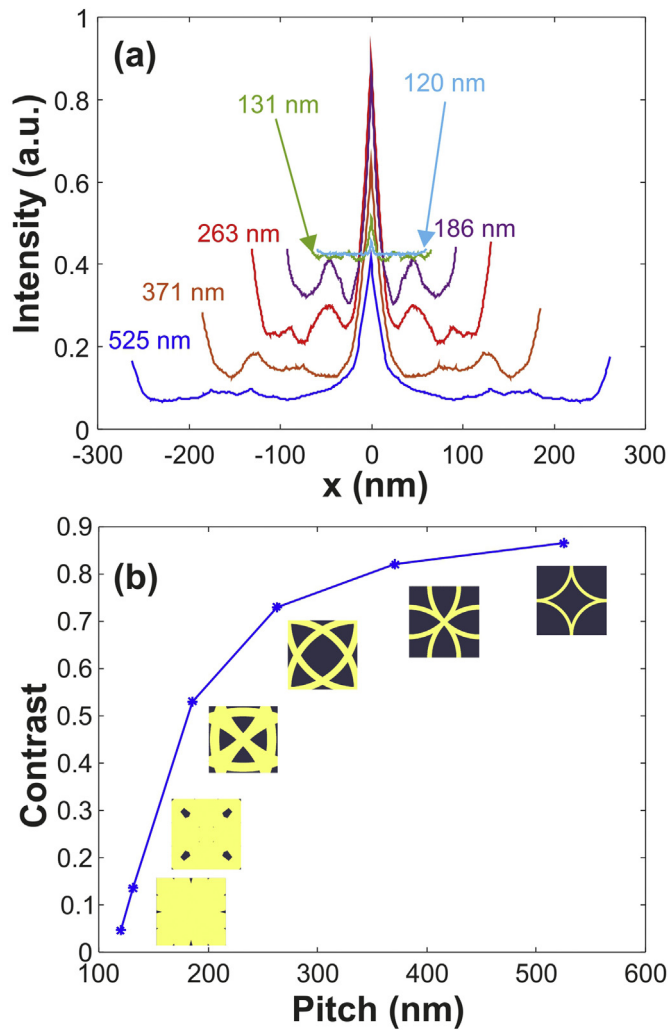
Fig. 3. (a) The simulated intensity of the dot along the horizontal axis for several pitches and (b) the simulated image contrast as a function of the pitch of the rings.

the ring determines the size of the printed dot and additionally by decreasing the ring width, we can enhance the contrast of our aerial image. Last, as it will be discussed in the following section, fabricating rings and crossed rings results into more stable intermediate structures during mask fabrication, which enables us to achieve smaller feature sizes.

3. Mask nanofabrication

The nanofabrication scheme of the transmission diffraction masks is outlined in Fig. 5. The transmission gratings are fabricated on thin and low-stress Si_3N_4 membranes of a thickness of about 80 nm and a calculated transmission of 50% at 13.5 nm wavelength. A Cr/Au/Cr metal thin film (5/20/5 nm) is then deposited as shown in Fig. 5 (a). Chromium is used as it is an excellent adhesion promoter (both for Au on the membrane and for HSQ on Au). Gold serves as a good seed layer for Ni electrochemical deposition. Subsequently a hydrogen silsesquioxane (HSQ) resist (~170 nm thick) is spin-coated onto the membranes and exposed into crossed or uncrossed annular rings by electron beam lithography (EBL) in a Raith EBPG 500+ system operated at 100 keV. The fracturing of the patterns for EBL as well as the beam stepping strategy are carefully chosen in order to avoid stitching errors in the subfield placement. Next, the samples are developed in a salty developer solution consisting of 1 part Microchemicals AZ 351B and 3 parts

deionized water and supercritically dried in order to avoid any pattern collapse due to capillary forces. The resulting rings are shown in the schematic of Fig. 5 (b). After removing the top chromium layer by Ar ion milling (Oxford Ionfab 300 plus), the membranes are immersed in a nickel sulphamate electroplating solution (pH of 3 and temperature of 57 °C) and a 150-nm-thick Ni film is grown on the Au seed layer around the HSQ mold in 8 min, as in Fig. 5 (c), using a Plating Electronic, PE86CB power supply (rectangular pulses of 2.0 s, with peak current density of 2.73 mA/cm^2 and 67% duty cycle). Nickel is an excellent choice of photon stop material, often used in the fabrication of X-ray optics, both due to its high absorbance and its relatively high diffraction efficiency, which does not vary significantly with thickness [16]. Finally, the HSQ is removed from the mask by etching in a buffered HF solution and the underlying Cr/Au/Cr layer that is not covered by the Ni layer is etched away by Ar ion milling (RF power of 400 W, a beam voltage of 300 V, beam current of 55 mA, and acceleration voltage of 350 V). The milling process is designed to fully etch the Cr/Au/Cr stack. As the milling process etches most materials and end detection is not available, it is possible that the Si_3N_4 membrane is also partially etched. However, overetching into the membrane would not pose a problem. On the contrary, thinning down the membrane would even increase its EUV transmission. The final mask with the Ni absorber is shown in Fig. 5 (d).

Figs. 5 (e)-(g) show typical scanning electron microscopy (SEM) images of the different steps during the nanofabrication process of a mask with crossed rings of a diameter of 525 nm, a ring width of 25 nm, and a pitch of 371 nm. In the image of Fig. 5 (e) HSQ rings are shown on the Cr/Au/Cr layer. In Fig. 5 (f), ~150 nm of Ni have been grown around the HSQ rings by electrochemical deposition. Finally in Fig. 5 (g) the final mask is shown with the HSQ rings and the underlying Cr/Au/Cr layer removed.

4. EUV exposures

To confirm the simulations on uncrossed rings reported in our previous work [10] and also on crossed rings shown in section 2 of this paper, we have performed ATL exposures at the XIL-II beamline of the SLS synchrotron (Paul Scherrer Institute) using EUV radiation at a wavelength of 13.5 nm with a bandwidth of about 4% and spatial coherence of more than 2 mm [17]. Spatial coherence of several millimeters is essential, as we have to perform our exposures at mask-wafer distances up to 1.1 mm (for the largest pitch). For example, with a plasma-based source with transverse coherence (spatial coherence) lengths up to 20 μm [12] our experiments would not be possible as coherence would be lost long before reaching the achromatic Talbot distance Z_A. All the exposures in this section were performed on thin (~35 nm) HSQ resist (Dow Corning XR1541 2%) spin-coated on 4" Si wafers at 5000 rpm for 45 s and no pre-exposure baking. Prior to spin-coating, the wafers were baked for 2 min at 180 °C for dehydration. After the exposure, the wafers were developed in a salty developer solution (Microchemicals AZ 351B 1 part, deionized water 3 parts) for 30 s.

In the first experiments, our goal was to verify the simulations of our previous work on non-intersecting rings, where an increase in mask efficiency was predicted for increasing ring diameter [10]. For this purpose, three different masks with 225, 325, and 425 nm diameter rings were used. The width of all the rings was 25 nm and the pitch of the rings on the mask was 500 nm, which corresponds to a pitch on wafer of 500 nm/$\sqrt{2} \cong 354$ nm. For all three masks an array of EUV doses was exposed and the efficiency of the masks was deduced from the doses to obtain a 40 nm diameter HSQ dot on the wafer. In fact, a large number of dots were analyzed with a particle analysis MATLAB code, which provided the mean diameter of the dots from the binarized grayscale SEM image. The mask-wafer distance was set to 1 mm, which is beyond the calculated $Z_A = 0.93$ mm for this pitch. This experiment is the first experimental demonstration of ATL masks with annular
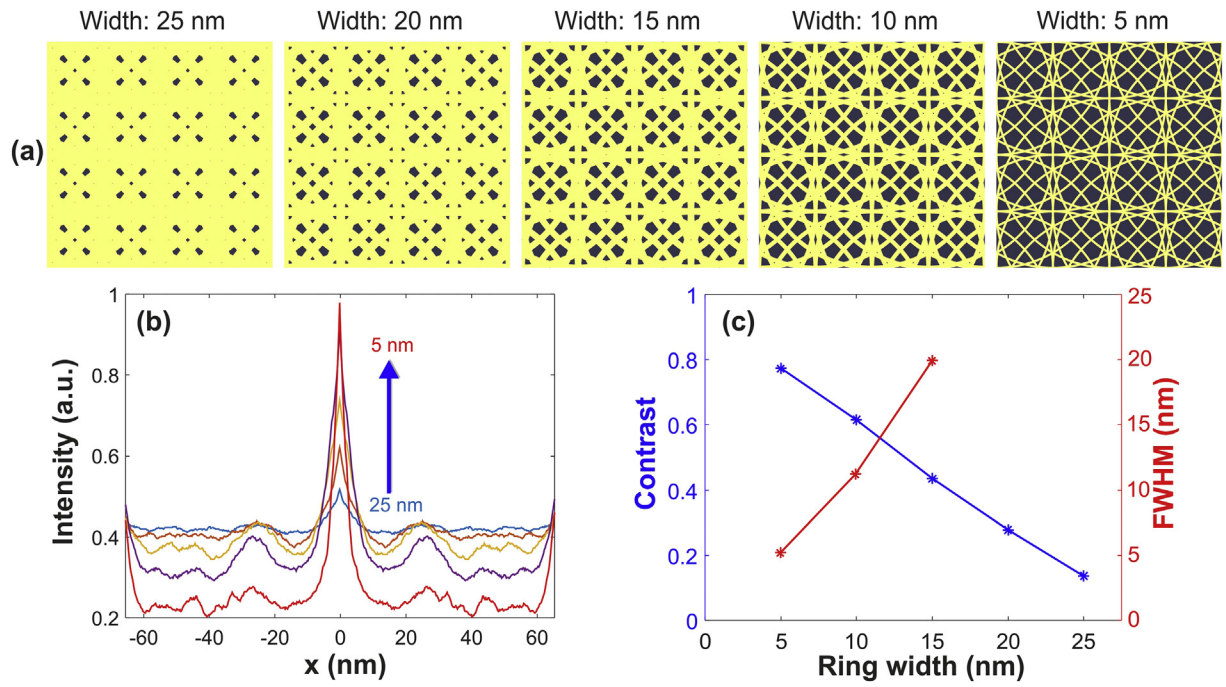
Fig. 4. (a) Mask layouts for rings of a pitch of 131 nm, the same mean diameter of 525 nm, but several ring width from 25 down to 5 nm. (b) The simulated intensity of the dot along the horizontal axis, calculated at a distance $z = 2z_A$ well within the achromatic regime. (c) The simulated image contrast as a function of the ring width. The FWHM values of the curves in (b) after normalizing them are also shown (right axis).
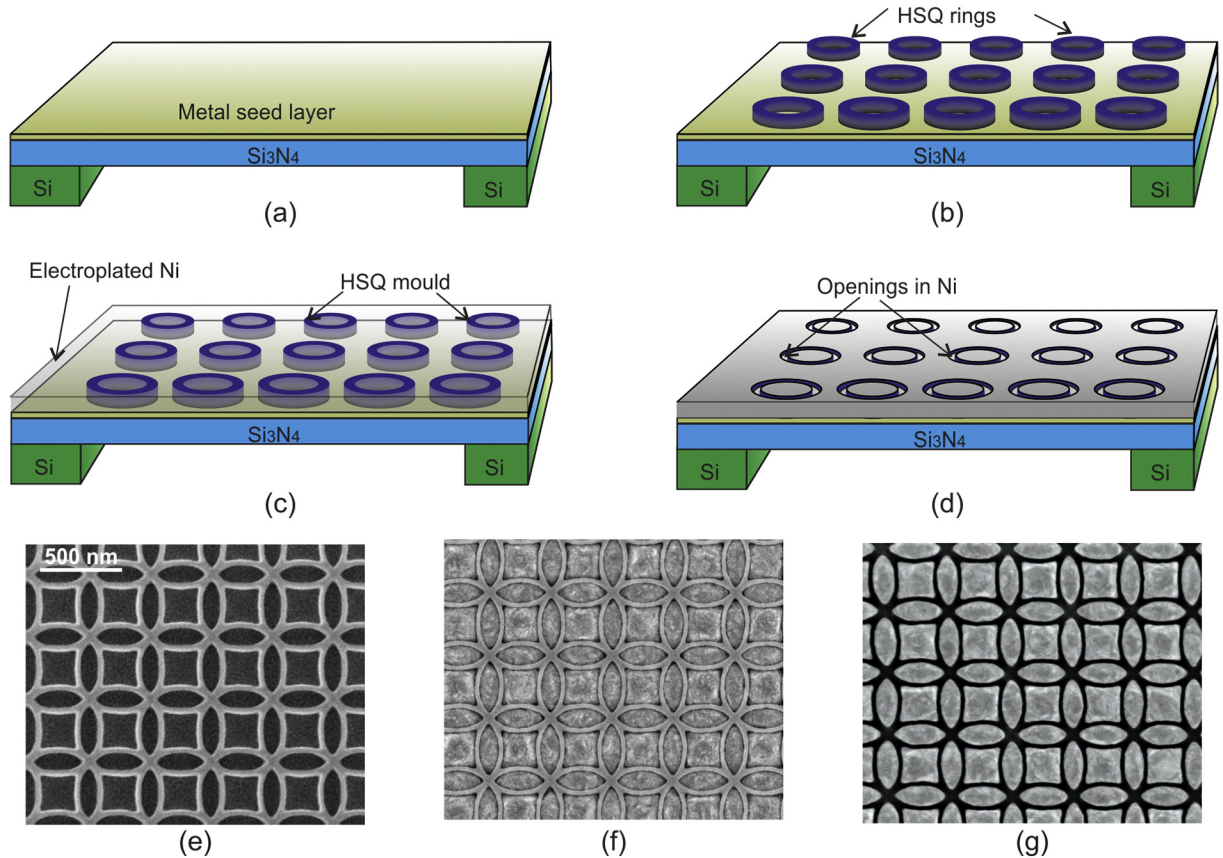
Fig. 5. Schematic of the mask nanofabrication and typical SEM images during the process. (a) Thin (~80 nm) suspended low-stress Si_3N_4 membrane covered with a thin Cr/Au/Cr seed layer. (b) HSQ-resist rings formed by EBL. (c) The HSQ rings serve as a mold for Ni electroplating. (d) The HSQ patterns as well as the underlying seed layer is etched away by a buffered HF etch followed by Ar ion milling. (e)-(g) SEM images of the mask corresponding to steps (b)-(d). The scale bar applies to all SEM images.
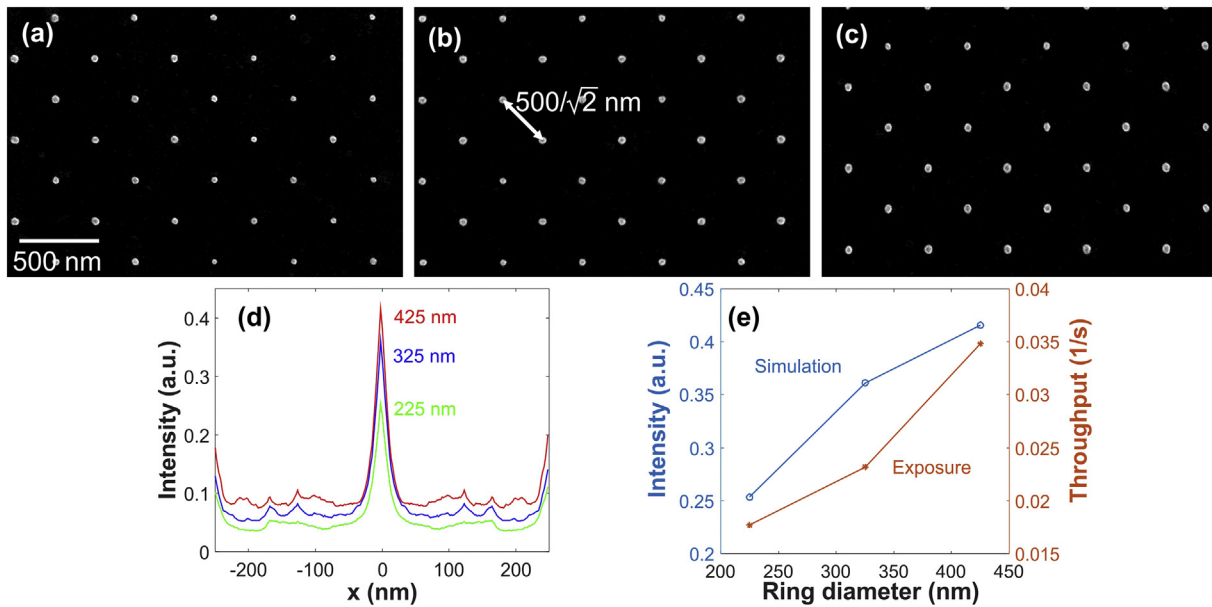
Fig. 6. The results of comparing masks with uncrossed rings of 500 nm pitch and 25 nm width. (a)-(c) SEM images of HSQ dots printed with EUV ATL lithography with masks with ring diameters of 425, 325, and 225 nm respectively. The exposures were performed at a mask-wafer distance of 1 mm, which is beyond the calculated $Z_A = 0.93$ mm for this pitch. (d) Simulated intensities of the aforementioned masks. (e) Qualitative comparison between the maxima of the simulated intensities and the exposure throughput as a function of the ring diameter.

openings that indeed produce arrays of dots. For all the different masks, dots with the expected pitch of 354 nm were produced. This is visualized in the SEM images of Fig. 6 (a)-(c), which show the HSQ dots of size ~40 nm for 425, 325, and 225 nm rings respectively. Fig. 6 (d) shows the simulated intensities of the dots versus the horizontal position for the three masks used in this experiment, with different ring sizes of 225, 325, and 425 nm in diameter, where an increase in intensity and therefore in throughput is found for the larger diameter rings. This is better understood in the plot of Fig. 6 (e), which shows the maximum intensities obtained from the simulations in (d) versus the ring diameter as well as the throughput of the actual exposures (defined as the inverse of the exposure time) also versus ring diameter. From this comparative plot it is evident that the predicted increase in throughput is indeed observed in the real EUV exposures.

In our second experiment, we verified that the masks with the crossed rings can indeed result in arrays of dots with the expected pitch (pitch on mask divided by $\sqrt{2}$). The results from three different masks are presented in Fig. 7. All masks are fabricated as in Fig. 5. The top images in Fig. 7 show part of the finished masks, corresponding to Fig. 5 (d) and the bottom ones are the SEM images of the respective EUV ATL exposures. The rings on the masks have a fixed diameter of 525 nm and a ring width of 25 nm, as shown in the inset of Fig. 7 (c). In Fig. 7 (a) the rings have a pitch of 525 nm (barely touching rings) while in Figs. 7 (b) and (c) the rings have a pitch of 371 nm and 228 nm respectively. From a mask nanofabrication point of view, all masks are well defined, even in the densely packed case of Fig. 7 (c). Upon EUV illumination, all three masks produce the expected aerial images which are shown in the SEM images at the bottom of Fig. 7. The mask-wafer distance for these exposures is set to 1.1 mm for pitch 525 nm, 0.6 mm for pitch 371 nm, and 0.3 mm for pitch 228 nm, which is about 100 μm beyond the respective Z_A. For all three cases, the pitch of the obtained dots is equal to the pitch of the rings on the mask divided by $\sqrt{2}$ and the dot arrays are rotated by 45° as predicted by the simulations in Figs. 1 and 2. In these experiments there was no attempt to push the resolution of the ATL method in terms of dot size. However, dot sizes down to about 33 nm, as shown in the inset of Fig. 7 (a), were achieved with no optimization of the process but only by reducing the exposure dose. In order to further reduce the dot size, thinner HSQ should be used and also an adhesion promoter to prevent pattern collapse, as for example the

SurPass 3000 (DisChem), which has previously been used to promote the adhesion between HSQ and spin-on-carbon [18].

5. Conclusions and outlook

In summary, we have performed extensive simulations of different ATL mask layouts with the goal of increasing the throughput of the ATL method. We have previously found that periodic dot arrays can be obtained by using masks with annular rings instead of holes. In this study, the simulations also show that the intensity of the main peaks in the aerial image scales with the ring size and at the same time the width of the ring has an effect on the size of the obtained dot. We have also shown that the rings on the masks can also be crossed and the ring pitch still defines the pitch of the dots in the aerial image. Although by reducing the pitch of the crossed rings we can achieve higher density dot arrays, this eventually results in loss of contrast in the aerial image. This can be compensated by reducing the width of the annular rings, which restores missing details on the masks due to the high density of the rings.

Several masks with rings and crossed rings were fabricated in a procedure involving several processing steps. The nanofabrication of masks with rings instead of holes has an additional significant advantage, besides the increase in the throughput: The nanofabrication of the masks is based on HSQ rings as in Fig. 5 (b). A conventional ATL mask with holes would require high aspect ratio HSQ pillars which suffer from collapse due to capillary forces, when the mask is introduced in the Ni electroplating solution. A ring (in fact a cylinder in three dimensions) is by design a more stable shape and pattern collapse is not observed.

The simulated results were confirmed by experimental data obtained by EUV exposures with synchrotron light. We confirmed that the masks with ring arrays produce dot arrays with the $\sqrt{2}$ demagnification and that larger rings lead to higher mask efficiencies, as predicted by the simulations. Furthermore the exposures with masks with crossed rings show that even in this case arrays of dots are obtained with the expected demagnification.

In the future, we aim for pushing the limits of resolution using masks with annular rings by reducing the pitch and also the ring width
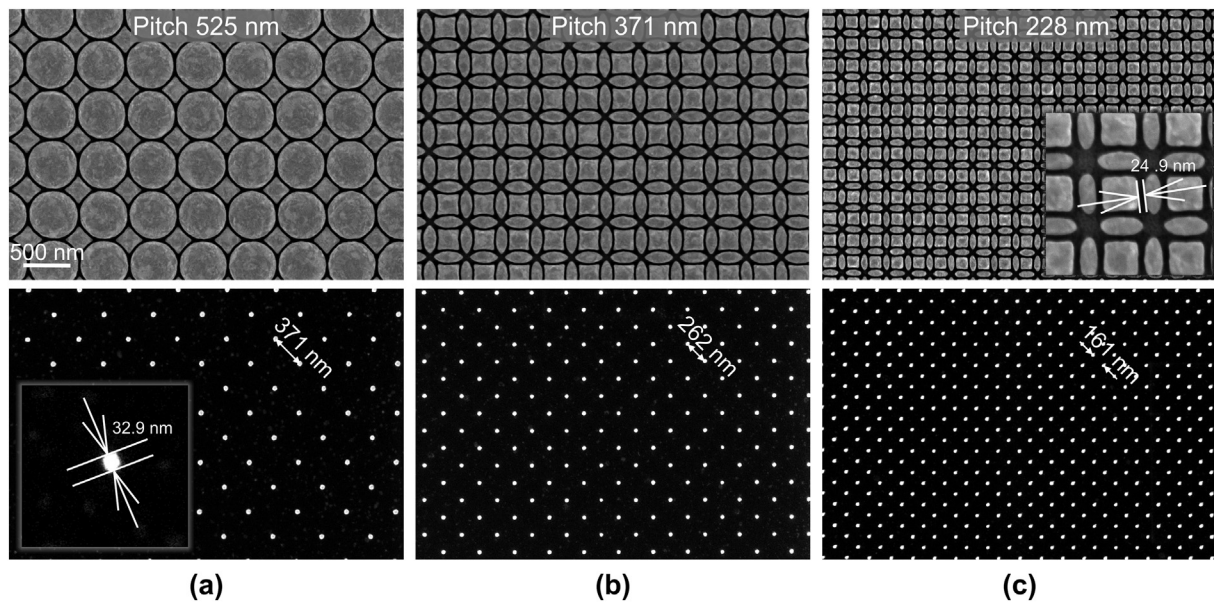
Fig. 7. SEM images of masks with crossed rings (top images) and the corresponding exposure results recorded on HSQ resist (bottom images). In all the cases, the rings have a diameter of 525 nm and a width of 25 nm. (a) Rings with pitch 525 nm (371 on wafer). (b) Rings with a pitch of 371 nm (262 on wafer). (c) Rings with a pitch of 228 nm (161 on wafer). In the inset of (a) we see the smallest dot obtained of 32.9 nm and in the inset of (c) the actual ring width of about 25 nm is shown. The mask-wafer distance for (a)-(c) is 1.1, 0.6, and 0.3 mm respectively.

to achieve smaller dots and pitches. It is not trivial to predict what the ultimate resolution or pitch might be, as this depends on several aspects, such as the materials used for the mask fabrication, the nanofabrication methods and in particular the resolution of EBL used to pattern the masks, and not the least on the performance of the EUV resists. From a theoretical perspective more rigorous simulations will definitely be needed. However, beyond the masks with rings, it is evident, that the ATL method has not been fully explored, and there is still work to be done to improve the resolution and the density of the features recorded on the resist. As the aerial image and the mask are not necessarily similar (for example a mask with rings produces an aerial image with sharp dots) we strongly believe there is a lot of room for more intelligent mask designs that can lead to efficient and high-resolution periodic patterning. This includes both simulations of different layouts and also revising the nanofabrication protocols, to be able to fabricate higher resolution masks. Being able to pattern versatile periodic structures at the nanoscale in an efficient manner and over large areas paves the way for several applications in research and development both in academic and industrial projects.

Declaration of Competing Interest

None.

Acknowledgements

References

[1] H. Duan, H. Hu, K. Kumar, Z. Shen, J.K.W. Yang, Direct and reliable patterning of plasmonic nanostructures with Sub-10-nm gaps, ACS Nano 5 (9) (2011) 7593–7600.

[2] R.M. De La Rue, C. Seassal, Photonic crystal devices: some basics and selected topics, Laser Photonics Rev. 6 (4) (2012) 564–597.

[3] B.D. Terris, T. Thomson, Nanofabricated and self-assembled magnetic structures as data storage media, J. Phys. D. Appl. Phys. 38 (12) (2005) R199–R222.

[4] P. Zhang, P. Liu, S. Siontas, A. Zaslavsky, D. Pacifici, J.-Y. Ha, S. Krylyuk, A.V. Davydov, Dense nanoimprinted silicon nanowire arrays with passivated axial p-i-n junctions for photovoltaic applications, J. Appl. Phys. 117 (12) (2015) 125104.

[5] S. Gottlieb, D. Kazazis, I. Mochi, L. Evangelio, M. Fernández-Regúlez, Y. Ekinci, F. Perez-Murano, Nano-confinement of block copolymers in high accuracy topographical guiding patterns: modelling the emergence of defectivity due to incommensurability, Soft Matter 14 (33) (2018) 6799–6808.

[6] A.I. Hochbaum, J. Aizenberg, Bacteria pattern spontaneously on periodic nanostructure arrays, Nano Lett. 10 (9) (2010) 3717–3721.

[7] X. Wang, L.-T. Tseng, D. Kazazis, Z. Tasdemir, M. Vockenhuber, I. Mochi, Y. Ekinci, Studying resist performance for contact holes printing using EUV interference lithography, J. Micro Nanolithogr. MEMS MOEMS 18 (1) (2019) 013501.

[8] H.H. Solak, Y. Ekinci, Achromatic spatial frequency multiplication: a method for production of nanometer-scale periodic structures, J. Vac. Sci. Technol. B 23 (6) (2005) 2705–2710.

[9] D.M. Tennant, Limits of conventional lithography, in: G. Timp (Ed.), Nanotechnology, Springer, New York, 1999, p. 164.

[10] D. Kazazis, L.-T. Tseng, Y. Ekinci, Improving the resolution and throughput of achromatic Talbot lithography, J. Vac. Sci. Technol. B 36 (6) (2018) 06J501.

[11] K. Bergmann, S.V. Danylyuk, L. Juschkin, Optimization of a gas discharge plasma source for extreme ultraviolet lithography at a wavelength of 11 nm, J. Appl. Phys. 106 (7) (2009) 073309.

[12] S. Brose, J. Tempeler, S. Danylyuk, P. Loosen, L. Juschkin, Achromatic Talbot lithography with partially coherent extreme ultraviolet radiation: process window analysis, J. Micro/Nanolithogr. MEMS MOEMS 15 (4) (2016) 043502.

[13] H. Kim, W. Li, M.C. Marconi, W.S. Brocklesby, L. Juschkin, Restorative self-image of rough-line grids: application to coherent EUV Talbot lithography, IEEE Photonics J. 8 (3) (2016) 1–9.

[14] H.F. Talbot, LXXVI. Facts relating to optical science. No. IV, Philos. Mag. 9 (56) (1836) 401–407.

[15] L. Rayleigh, XXV. On copying diffraction-gratings, and on some phenomena connected therewith, Philos. Mag. 11 (67) (1881) 196–205.

[16] W. Karim, S.A. Tschupp, M. Oezaslan, T.J. Schmidt, J. Gobrecht, J.A. van Bokhoven, Y. Ekinci, High-resolution and large-area nanoparticle arrays using EUV interference lithography, Nanoscale 7 (16) (2015) 7386–7393.

[17] N. Mojarad, J. Gobrecht, Y. Ekinci, Interference lithography at EUV and soft X-ray wavelengths: principles, methods, and applications, Microelectron. Eng. 143 (2015) 55–63.

[18] L.-T. Tseng, D. Kazazis, X. Wang, C.M. Popescu, A.P.G. Robinson, Y. Ekinci, Sub-20 nm Si fins with high aspect ratio via pattern transfer using fullerene-based spin-on-carbon hard masks, Microelectron. Eng. 210 (2019) 8–13.